Co-published by
Institute of Fluid-Flow Machinery
Polish Academy of Sciences
Committee on Thermodynamics and Combustion
Polish Academy of Sciences

Copyright©2026 by the Authors under licence CC BY-NC-ND 4.0

http://www.imp.gda.pl/archives-of-thermodynamics/

Experimental test and simulation of properties from ternary Bi-Ni-Pb system: microstructural, mechanical, electrical properties, Scheil and Lever simulation

Veljko Minic[a], Nikola Bojanic[a], Milena Zecevic[a*], Aleksandar Djordjevic[a], Dragan Manasijevic[b], Milan Kolarevic[c]

[a]Faculty of Technical Science, Department of Technological Engineering, University of Prishtina in Kosovska Mitrovica, Kneza Milosa 7, Kosovska Mitrovica, Kosovo[**]
[b]Technical Faculty in Bor, University of Belgrade, VJ 12, 19210 Bor, Serbia
[c]Faculty of Mechanical and Civil Engineering in Kraljevo,University of Kragujevac, Kraljevo, Serbia
[*]Corresponding author email: milena.premovic@gmail.com, [**]UNSCR 1244

Received: 24.04.2026; revised: 14.08.2026; accepted: 10.09.2026

Abstract

Due to the wide application of nickel alloys, the ternary Bi-Ni-Pb system was experimentally investigated. The microstructure, Brinell hardness, and electrical conductivity of 15 ternary alloys were examined. The prepared alloys were selected from three vertical sections: Bi-NiPb, Ni-BiPb and Pb-BiNi. The observed microstructures were compared with the calculated isothermal section at 25°C, and good agreement was achieved. Brinell hardness was measured at three different points on each sample, and the mean values were used to predict hardness across the entire composition range. Hardness prediction was performed using a mathematical model developed through ANOVA analysis. Among the investigated ternary alloys, $Bi_{40}Ni_{40}Pb_{20}$ and $Bi_5Ni_{90}Pb_5$ exhibited the highest hardness values. Electrical conductivity was measured at four different points on each sample, and the mean values were used to predict electrical conductivity throughout the composition range. The $Bi_5Ni_{90}Pb_5$ alloy showed the highest electrical conductivity among all tested ternary alloys. Furthermore, Scheil and Lever simulations were performed for the $Bi_5Ni_{90}Pb_5$ alloy, which exhibited the most favourable combination of mechanical and electrical properties.

Keywords: Mechanical properties; Electrical properties; Microstructural properties; Scheil and Lever simulation; Ternary Bi-Ni-Pb system

Vol. 47(2026), No. 3, 213–232; doi: 10.24425/ather.2026.7520

Cite this manuscript as: Minic, V., Bojanic, N., Zecevic, M., Djordjevic, A., Manasijevic, D., & Kolarevic, M. (2026). Experimental test and simulation of properties from ternary Bi-Ni-Pb system: microstructural, mechanical, electrical properties, Scheil and Lever simulation. *Archives of Thermodynamics*, 47(3), 213–232.

1. Introduction

Nickel and nickel-based alloys have been extensively studied in the literature [1–3] due to their wide range of industrial applications, including lead wires, battery components, transducers, spark electrodes and heat exchangers. In addition to nickel, both bismuth [4] and lead [5] have attracted considerable scientific interest because of their unique physical and chemical properties. Bismuth-based alloys are widely recognised as environmentally friendly alternatives to lead-containing materials because of their low toxicity, low melting temperature and favourable casting behaviour. The addition of nickel to Bi-Pb alloys

may significantly modify the phase constitution, mechanical properties, electrical conductivity and solidification behaviour, making these ternary alloys attractive for applications requiring tailored combinations of physical and mechanical properties.

Previous investigations of the Bi-Ni-Pb system and related ternary alloy systems have primarily focused on phase equilibria, thermodynamic assessment and microstructural characterisation. Reliable knowledge of phase relationships is essential for understanding alloy behaviour and for predicting the formation of equilibrium and non-equilibrium phases during solidification. However, considerably less attention has been devoted to correlating alloy composition and phase constitution with mechanical and electrical properties, although these characteristics are of primary importance for the practical application and optimisation of multicomponent alloys.

The ternary Bi-Ni-Pb system was previously investigated by our research group [6]. The reported results focused on the experimental determination of phase equilibria. The studied alloys were used to establish phase relationships along three vertical sections (x(Bi) = 0.75, x(Ni) = 0.10, and x(Pb) = 0.90) as well as two isothermal sections at 100°C and 300°C. Based on these results, a reliable thermodynamic description of the ternary Bi-Ni-Pb system was developed in Ref. [6], and this thermodynamic database was employed in the present study.

In recent years, statistical approaches such as response surface methodology (RSM) and mixture experimental designs have become valuable tools in materials science for establishing quantitative relationships between alloy composition and material properties. Unlike conventional factorial designs, mixture designs explicitly account for the compositional constraint that the sum of all components is constant. These methods enable efficient optimisation of multicomponent alloy systems, reduce the number of required experiments and provide predictive mathematical models for engineering applications. Their application has been successfully demonstrated for the optimisation of mechanical, electrical, thermal and corrosion properties of metallic materials.

In the current work, fifteen ternary alloys were prepared and subjected to various experimental investigations. Their microstructures were characterised using light optical microscopy (LOM) and scanning electron microscopy (SEM). The chemical compositions of the alloys and their constituent phases were determined by energy-dispersive spectroscopy (EDS), while phase identification was performed using X-ray diffraction (XRD) analysis.

The experimental SEM-EDS and XRD results were compared with the calculated isothermal section at 25°C, showing good agreement between the experimental observations and thermodynamic predictions. The isothermal section at 25°C was calculated using the Pandat software [7].

Hardness and electrical conductivity were measured on the same set of alloys. Since these properties are strongly influenced by alloy composition, phase distribution and microstructure, predictive modelling can provide valuable guidance for alloy design while reducing experimental effort. The average values obtained from the experimental measurements were therefore used for mathematical modelling based on response surface methodology and mixture design. In addition, Scheil and Lever simulations were performed for the $Bi_5Ni_{90}Pb_5$ alloy using Pandat software to evaluate their solidification behaviour and to compare equilibrium and non-equilibrium solidification paths with the experimentally observed microstructures.

The novelty of the present work lies in the combined experimental, thermodynamic and statistical investigation of the Bi-Ni-Pb ternary system. By integrating phase-equilibria calculations, microstructural characterisation, mechanical and electrical property measurements, response surface modelling and solidification simulations, the study establishes quantitative composition-structure-property relationships that may facilitate the design and optimisation of Bi-Ni-Pb alloys for future engineering applications.

2. Materials and methods

2.1. Experimental procedure

A total of fifteen ternary and three binary alloy samples were prepared from high-purity elemental materials (Bi, Ni and Pb, 99.999 at. %) supplied by Alfa Aesar, Germany. The experimental compositions were selected to achieve the broadest possible coverage of the ternary compositional space, thereby ensuring representative sampling of the system. The mass of each ternary alloy sample was approximately 5 g. The accurately weighed amounts of the constituent elements were melted using an arc-melting furnace under a high-purity argon atmosphere with a non-consumable tungsten electrode. To ensure sufficient mixing and chemical homogeneity, each sample was remelted five times. After the final melting step, the alloys were slowly cooled to room temperature. The average mass loss during the melting process was approximately 0.5% of the initial sample mass. The nominal compositions of the prepared alloys are listed in Table 1.

The nominal compositions of the investigated alloys were chosen along three vertical sections of the Bi-Ni-Pb ternary system. Specifically, samples 1–5 were located on the Bi-NiPb section, samples 6–11 on the Ni-BiPb section, and samples 12–15 on the Pb-BiNi section, enabling systematic investigation of the influence of composition on the microstructure and measured properties.

The prepared samples were divided into two groups according to the planned characterisation methods. The first group was subjected to XRD analysis for phase identification, while the second group was used for microstructural characterisation by LOM and SEM-EDS, as well as for electrical conductivity and hardness measurements.

For X-ray diffraction (XRD) analysis, the selected samples were mechanically crushed and ground into fine powders. Powder XRD patterns were collected using a D2 PHASER diffractometer (Bruker, Karlsruhe, Germany) equipped with a dynamic scintillation detector and a ceramic Cu X-ray tube (KFL-Cu-2K). The measurements were performed in the 2θ range from 5° to 75° with a step size of 0.02°. Phase identification was carried out using the TOPAS 4.2 software package and the ICDD PDF-2 database (2013). The diffractometer was calibrated using the Bruker standard Korundprobe A26-B26-S. In addition, ten high-purity elemental powders purchased from

Table 1. Nominal composition of Bi-Ni-Pb alloys used for experimental tests.

Number (mark of sample)	Alloy nominal composition (mole fraction)		
	Bi	Ni	Pb
B1	0	0.5	0.5
1	0.2	0.4	0.4
2	0.4	0.3	0.3
3	0.5	0.25	0.25
4	0.6	0.2	0.2
5	0.8	0.1	0.1
B2	0.5	0	0.5
6	0.45	0.1	0.45
7	0.4	0.2	0.4
8	0.35	0.3	0.35
9	0.3	0.4	0.3
10	0.1	0.8	0.1
11	0.05	0.9	0.05
B3	0.5	0.5	0
12	0.4	0.4	0.2
13	0.3	0.3	0.4
14	0.2	0.2	0.6
15	0.1	0.1	0.8

Alfa Aesar were used as reference materials during the calibration procedure to ensure accurate phase identification and reliable diffraction data analysis.

The samples from the second group were prepared for metallographic examination following a standard preparation procedure. The samples were initially embedded in a polymer resin, followed by sequential grinding using SiC abrasive papers and polishing with diamond paste to obtain a smooth and scratch-free surface. After polishing, the samples were cleaned in an ultrasonic bath to remove any residual contaminants. The prepared specimens were subsequently used for LOM, Brinell hardness and electrical conductivity measurements. For SEM-EDS analysis, the polymer resin was carefully removed after metallographic preparation to expose the sample surface and enable accurate microstructural observation and chemical composition analysis.

The microstructures of the prepared alloys were examined using a light optical microscope (Olympus GX23, Olympus Corporation, Japan). The observations were performed on metallographically prepared surfaces after grinding, polishing, and ultrasonic cleaning.

Hardness measurements were performed using a Brinell hardness tester (INNOVATEST, model NEXUS 3001) according to the ISO 6506 standard. A spherical carbide indenter with a diameter of 2.5 mm was used, and the applied indentation load was 306.4 N for 10 s. The measurements were carried out on metallographically prepared surfaces under controlled conditions. For each alloy, hardness was measured at three different locations to account for possible microstructural heterogeneity, and the average value was calculated and used for further analysis and mathematical modelling. The distance between individual indentations was selected to minimise the influence of neighbouring imprints and to ensure reliable hardness measurements. The Brinell hardness values were determined automatically by the instrument based on the measured indentation diameter.

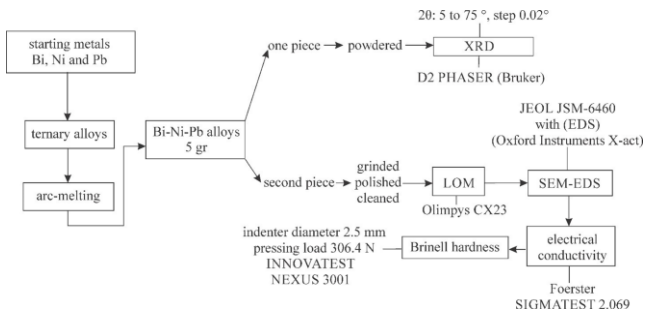


Fig. 1. Scheme of the experimental procedure with the conditions and type of used devices.

Electrical conductivity measurements were carried out using a Foerster SIGMATEST 2.069 eddy current instrument. The measurements were performed at room temperature on metallographically prepared samples with a flat and clean surface to ensure good contact between the probe and the sample. For each alloy, the electrical conductivity was measured at four different positions, and the average value was calculated and used for further analysis and mathematical modelling. Before measurements, the instrument was calibrated using the appropriate reference standards according to the manufacturer's recommendations. The results were expressed in MS/m, and the measurement procedure was performed under identical conditions for all investigated samples to ensure reliable comparison of the electrical conductivity values.

SEM–EDS analysis was performed using a JEOL JSM-6460 scanning electron microscope equipped with an Oxford Instruments X-act EDS detector. Before the measurements, the EDS system was calibrated using a pure copper (Cu) standard to ensure accurate elemental identification and quantitative chemical analysis.

EDS elemental mapping was initially performed to evaluate the compositional homogeneity of the investigated samples and to identify possible elemental segregation. Subsequently, the overall chemical compositions of the alloys and the compositions of individual coexisting phases were determined by EDS point and area analyses. The compositions of the coexisting phases were obtained by analysing several regions corresponding to the same phase in different areas of each sample, providing more reliable compositional values and reducing the influence of local microstructural variations.

A schematic overview of the complete experimental procedure, including sample preparation and subsequent characterisation steps, is presented in Fig. 1.

Experimental results from Brinell hardness and electrical conductivity measurements were used to develop mathematical models describing these properties across the entire compositional range.

2.2. Statistical methodology

The statistical methodology adopted for developing and validating the predictive mixture models is summarised in Fig. 2. The

workflow consisted of five consecutive stages: (i) model selection, (ii) statistical evaluation, (iii) diagnostic analysis, (iv) model visualisation and (v) model validation. This procedure was applied independently to both investigated responses, hardness and electrical conductivity, ensuring a consistent statistical treatment throughout the study [8–10].

The experimental data were analysed using Design-Expert® software (Version 9.0.6, Stat-Ease Inc., Minneapolis, MN, USA) [11]. Scheffé mixture models of increasing complexity (linear, quadratic, special cubic, cubic, special quartic and quartic) were fitted to the experimental data [10,12–14]. For a three-component mixture satisfying the constraint $x_1+x_2+x_3=1$, the investigated Scheffé mixture models can be written as follows [10,12,14]:

Linear: $$\hat{y} = \sum_{i=1}^{q} \beta_i x_i, \quad (1)$$

Quadratic: $$\hat{y} = \sum_{i=1}^{q} \beta_i x_i + \sum_{i<j}^{q-1} \sum_{j}^{q} \beta_{ij} x_i x_j, \quad (2)$$

Special Cubic: $$\hat{y} = \sum_{i=1}^{q} \beta_i x_i + \sum_{i<j}^{q-1} \sum_{j}^{q} \beta_{ij} x_i x_j + \sum_{i<j}^{q-2} \sum_{j<k}^{q-1} \sum_{k}^{q} \beta_{ijk} x_i x_j x_k, \quad (3)$$

Full Cubic: $$\hat{y} = \sum_{i=1}^{q} \beta_i x_i + \sum_{i<j}^{q-1} \sum_{j}^{q} \beta_{ij} x_i x_j + \sum_{i<j}^{q-1} \sum_{j}^{q} \delta_{ij} x_i x_j (x_i - x_j) + \sum_{i<j}^{q-2} \sum_{j<k}^{q-1} \sum_{k}^{q} \beta_{ijk} x_i x_j x_k, \quad (4)$$

Special Quartic:

$$\hat{y} = \sum_{i=1}^{q} \beta_i x_i + \sum_{i<j}^{q-1} \sum_{j}^{q} \beta_{ij} x_i x_j + \sum_{i<j}^{q-2} \sum_{j<k}^{q-1} \sum_{k}^{q} \beta_{iijk} x_i^2 x_j x_k + \sum_{i<j}^{q-2} \sum_{j<k}^{q-1} \sum_{k}^{q} \beta_{ijjk} x_i x_j^2 x_k + \sum_{i<j}^{q-2} \sum_{j<k}^{q-1} \sum_{k}^{q} \beta_{ijkk} x_i x_j x_k^2, \quad (5)$$

Full Quartic:

$$\hat{y} = \sum_{i=1}^{q} \beta_i x_i + \sum_{i<j}^{q-1} \sum_{j}^{q} \beta_{ij} x_i x_j + \sum_{i<j}^{q-1} \sum_{j}^{q} \delta_{ij} x_i x_j (x_i - x_j) + \sum_{i<j}^{q-1} \sum_{j}^{q} \gamma_{ij} x_i x_j (x_i - x_j)^2 + \sum_{i<j}^{q-2} \sum_{j<k}^{q-1} \sum_{k}^{q} \beta_{iijk} x_i^2 x_j x_k +$$
$$+ \sum_{i<j}^{q-2} \sum_{j<k}^{q-1} \sum_{k}^{q} \beta_{ijjk} x_i x_j^2 x_k + \sum_{i<j}^{q-2} \sum_{j<k}^{q-1} \sum_{k}^{q} \beta_{ijkk} x_i x_j x_k^2 + \sum_{i<j}^{q-3} \sum_{j<k}^{q-2} \sum_{k<l}^{q-1} \sum_{l}^{q} \beta_{ijkl} x_i x_j x_k x_l. \quad (6)$$

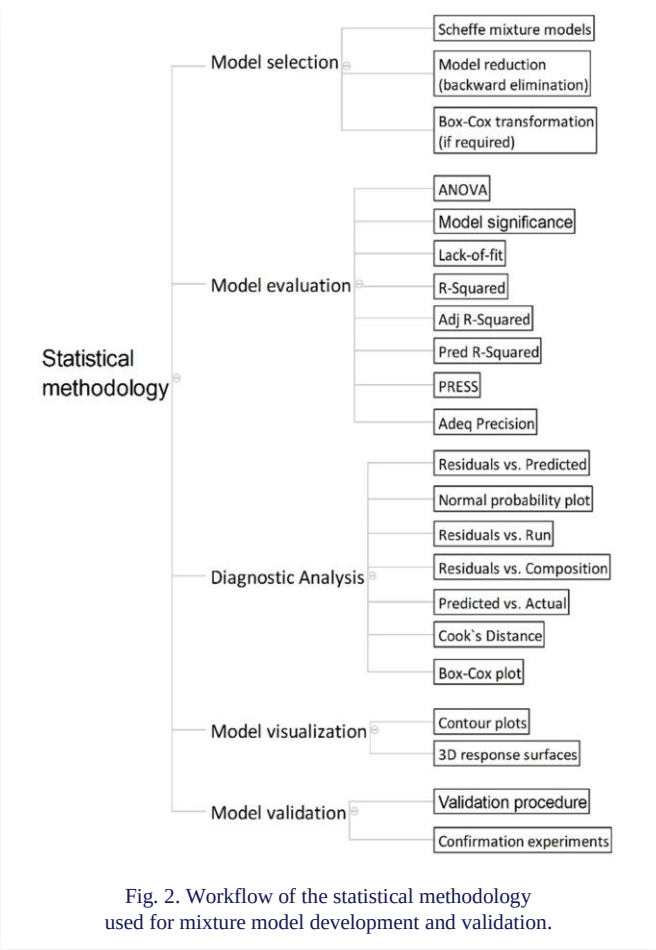


Fig. 2. Workflow of the statistical methodology used for mixture model development and validation.

The candidate Scheffé mixture models were fitted sequentially, and only hierarchical models were considered during model selection. Model reduction was performed using backward elimination with a significance level of $\alpha = 0.05$ while preserving model hierarchy [9,15]. Whenever necessary, a Box-Cox transformation was considered to improve model adequacy; however, no transformation was required for the final models [9,12].

The candidate models were statistically evaluated using analysis of variance (ANOVA) [9,15]. Model significance was assessed by the F-test and associated p-values, whereas goodness-of-fit was evaluated using the coefficient of determination (R^2), adjusted coefficient of determination (Adj. R^2), predicted coefficient of determination (Pred. R^2), predicted residual sum of squares (PRESS), adequate precision and the lack-of-fit test [8,9,11]. The final model for each response was selected by considering both statistical significance and predictive capability rather than relying on a single statistical criterion.

Model adequacy was further examined through residual diagnostics [9,11,15]. Diagnostic plots included predicted versus actual values, residuals versus predicted values, normal probability plots of residuals, residuals versus run order, residuals versus alloy composition, Cook's distance and Box-Cox plots. These analyses were used to verify the assumptions of normality, homoscedasticity, independence of residuals and the absence of influential observations.

The selected models were subsequently visualised using contour plots to illustrate the effects of alloy composition on the investigated responses and to identify regions exhibiting desirable combinations of properties within the experimental design space [8,9,12].

Finally, model validation was carried out by comparing predicted values with independent confirmation experiments performed at selected alloy compositions that were not included in model construction [8,9,11]. The agreement between experimental and predicted values was evaluated using the relative

prediction error, thereby demonstrating the predictive accuracy and practical applicability of the developed mixture models.

3. Results and discussion

Based on the thermodynamic assessment of the ternary Bi-Ni-Pb system reported in Ref. [6], six solid phases and one liquid phase are expected to exist. The identified solid phases and their corresponding crystallographic information are listed in Table 2.

Samples 2–4, 7, and 8 were found to contain the equilibrium phases Bi_3Ni, BiNi and (Pb), as identified by XRD and confirmed by EDS analysis. Their positions in the calculated isothermal section (Fig. 3) are consistent with the BiNi+Bi_3Ni+(Pb) three-phase equilibrium region. Sample 5 was characterised by the equilibrium phases Bi_3Ni, (Pb) and (εPb).

Table 2. Considered phase and their crystal structure data.

Phase names	Common names	Temperature, °C	Composition range in at. %	Strukturbericht symbol and Pearson symbol	Space group	Lattice parameters, Å	Ref.
RHOMBO_A7	(Bi)	0–271	100 Bi	*A7* *hR2*	$R\bar{3}m$	*a*=*b*=4.548, *c*=11.852	[16]
FCC_A1	(Ni) (Pb)	0–1455 0–327	97.80–100 Ni 96.88–100 Pb	*A1* *cF4*	$Fm\bar{3}m$	*a*=*b*=*c*=3.5243 *a*=*b*=*c*=4.9496	[17] [18]
HCP_A3	(εPb)	0–183.64	57.30–75.60 Pb	*A3*	$P6_3/mmc$	*a*=*b*=3.265 *c*=5.387	[19]
BI3NI	Bi_3Ni	0–464.83	25 Ni, 75Bi	*C4* *oP16*	*Pnma*	*a*=8.879 *b*=4.0998 *c*=11.483	[20]
BINI	BiNi	0–645.8	48.47–49.95 Ni	$B8_1$ *mC64*	*F*12/*m*1	*a*=14.124 *b*=8.1621 *c*=21.429	[21]

3.1. Microstructural properties

Fifteen slowly cooled ternary alloys (samples 1–15, listed in Table 1) were experimentally characterised. Their microstruc-tures were examined by LOM and SEM. The chemical compo-sitions of both the bulk alloys and the coexisting phases were determined using EDS. Phase identification was performed by XRD, and the combined EDS and XRD results are summarised in Table 3. The experimental findings were further validated by comparison with the calculated isothermal section of the Bi-Ni-Pb system at 25°C, shown in Fig. 3.

The experimentally determined alloy compositions obtained by EDS are superimposed on the calculated isothermal section as square markers. Excellent agreement was observed between the nominal alloy compositions and those measured by EDS, confirming the reliability of the alloy preparation procedure. To distinguish the three investigated vertical sections, different marker colours were used in Fig. 3. Red squares represent samples 1–5 from the Bi-NiPb vertical section, orange squares correspond to samples 6–11 from the Ni-BiPb vertical section, and green squares denote samples 12–15 from the Pb-BiNi vertical section.

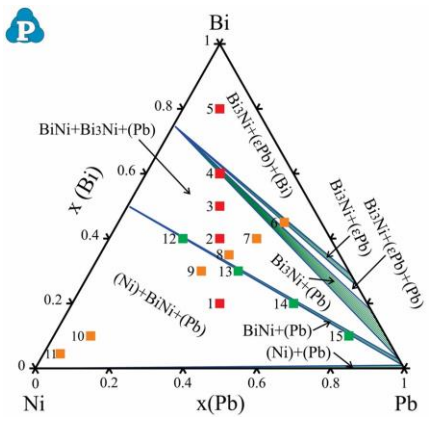


Fig. 3. Predicted isothermal section at 25°C with marked compositions of tested alloys.

The calculated isothermal section at 25°C comprises eight phase fields, including four two-phase and four three-phase equilibrium regions. The experimentally identified phase constitutions are fully consistent with the calculated phase equilibria, demonstrating good agreement between the thermodynamic predictions and the experimental observations.

XRD analysis showed that samples 1 and 9–15 consisted of the three equilibrium phases (Ni), BiNi and (Pb). The phase identification was confirmed by EDS analysis, and the corresponding phase compositions are listed in Table 3. As shown in Fig. 3, these samples are located within the three-phase equilibrium region (Ni)+BiNi+(Pb).

The experimental phase assemblage determined by XRD and EDS is in excellent agreement with the calculated isothermal section, confirming that the alloy belongs to the Bi_3Ni+(Pb)+(εPb) three-phase region.

Similarly, sample 6 was found to consist of the equilibrium phases Bi_3Ni, (Pb) and (εPb). The phases predicted by the calculated isothermal section were confirmed by both XRD and EDS analyses, demonstrating excellent agreement between the experimental observations and thermodynamic calculations.

Consequently, all four predicted three-phase equilibrium regions were experimentally validated. Moreover, the measured phase compositions closely matched the equilibrium compositions predicted by the thermodynamic calculations, further confirming the reliability of the thermodynamic description of the Bi-Ni-Pb system.

Table 3. EDS and XRD results of the ternary Bi-Ni-Pb samples.

Number	Composition of samples in at. %	Predicted phases	Determined phases		Compositions of phases in at. % determined by EDS		
			EDS	XRD	x(Bi)	x(Ni)	x(Pb)
1	20.19 Bi 39.86 Ni 39.95 Pb	(Ni) BiNi (Pb)	(Ni) BiNi (Pb)	(Ni) BiNi (Pb)	0.13 49.53 1.10	99.85 50.43 0.66	0.02 0.04 98.24
2	39.81 Bi 30.19 Ni 30.00 Pb	Bi_3Ni BiNi (Pb)	Bi_3Ni BiNi (Pb)	Bi_3Ni BiNi (Pb)	74.65 49.18 3.14	25.17 50.79 0.72	0.18 0.03 96.14
3	50.21 Bi 25.13 Ni 24.66 Pb	Bi_3Ni BiNi (Pb)	Bi_3Ni BiNi (Pb)	Bi_3Ni BiNi (Pb)	75.12 50.01 3.41	24.79 49.88 0.07	0.09 0.11 96.52
4	59.59 Bi 20.52 Ni 19.89 Pb	Bi_3Ni BiNi (Pb)	Bi_3Ni BiNi (Pb)	Bi_3Ni BiNi (Pb)	75.67 49.32 3.09	24.22 50.59 0.37	0.11 0.09 96.54
5	80.13 Bi 9.81 Ni 10.06 Pb	(Bi) BiNi (εPb)	(Bi) BiNi (εPb)	(Bi) BiNi (εPb)	98.72 50.92 29.87	1.13 48.99 1.00	0.15 0.09 69.13
6	45.12 Bi 9.91 Ni 44.97 Pb	Bi_3Ni (Pb) (εPb)	Bi_3Ni (Pb) (εPb)	Bi_3Ni (Pb) (εPb)	74.25 18.82 25.18	25.72 0.09 0.02	0.03 81.09 74.80
7	39.18 Bi 20.81 Ni 40.01 Pb	Bi_3Ni BiNi (Pb)	Bi_3Ni BiNi (Pb)	Bi_3Ni BiNi (Pb)	74.65 49.97 3.28	25.15 49.88 0.02	0.20 0.15 96.70
8	35.23 Bi 30.17 Ni 34.60 Pb	Bi_3Ni BiNi (Pb)	Bi_3Ni BiNi (Pb)	Bi_3Ni BiNi (Pb)	75.62 49.74 3.19	24.36 50.15 0.04	0.02 0.11 96.77
9	29.81 Bi 40.15 Ni 30.04 Pb	(Ni) BiNi (Pb)	(Ni) BiNi (Pb)	(Ni) BiNi (Pb)	0.18 50.13 0.92	99.70 49.79 0.05	0.12 0.08 99.03
10	9.83 Bi 80.54 Ni 9.63 Pb	(Ni) BiNi (Pb)	(Ni) BiNi (Pb)	(Ni) BiNi (Pb)	0.07 50.23 1.03	99.75 49.72 0.26	0.18 0.05 98.71
11	5.12 Bi 90.03 Ni 4.85 Pb	(Ni) BiNi (Pb)	(Ni) BiNi (Pb)	(Ni) BiNi (Pb)	0.18 49.87 0.98	99.65 50.08 0.37	0.17 0.05 98.65
12	40.71 Bi 39.58 Ni 19.71 Pb	(Ni) BiNi (Pb)	(Ni) BiNi (Pb)	(Ni) BiNi (Pb)	0.15 49.93 0.84	99.77 49.98 0.74	0.08 0.09 98.42
13	30.64 Bi 30.02 Ni 39.34 Pb	(Ni) BiNi (Pb)	(Ni) BiNi (Pb)	(Ni) BiNi (Pb)	0.03 50.07 1.01	99.92 49.82 0.21	0.05 0.11 98.78
14	20.66 Bi 19.82 Ni 59.52 Pb	(Ni) BiNi (Pb)	(Ni) BiNi (Pb)	(Ni) BiNi (Pb)	0.12 49.42 0.97	99.81 50.52 0.50	0.07 0.06 98.53
15	9.92 Bi 10.11 Ni 79.97 Pb	(Ni) BiNi (Pb)	(Ni) BiNi (Pb)	(Ni) BiNi (Pb)	0.15 49.87 0.89	99.79 50.04 0.70	0.06 0.09 98.41

The microstructures of samples 1 and 3 are presented in Fig. 4. Three distinct phases can be clearly distinguished in both micrographs, and the corresponding phases are labelled directly on the images. In both microstructures, the (Pb) phase forms the continuous matrix in which the other two phases are dispersed.

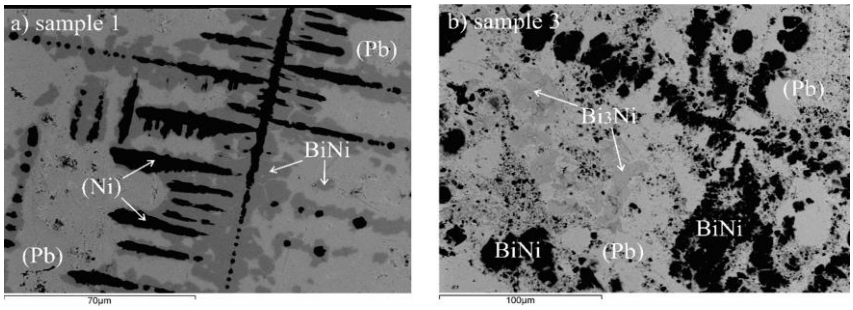


Fig. 4. SEM micrographs of the samples: a) 1; b) 3.

In the microstructure of sample 1, the (Ni) phase appears as a dark contrast phase with clearly defined boundaries, while the BiNi phase exhibits a light-gray contrast and is mainly located in the vicinity of the (Ni) phase. Such a phase arrangement indicates a close spatial relationship between the intermetallic BiNi phase and the Ni-rich regions formed during solidification.

In the microstructure of sample 3, the Bi_3Ni and BiNi phases exhibit similar morphologies and distribution patterns within the (Pb) matrix. The Bi_3Ni phase appears with a dark-gray contrast, whereas the BiNi phase is observed as a darker phase, which can be attributed to the higher Ni content and differences in chemical composition between these intermetallic compounds. The observed phase morphology and distribution are consistent with the phase equilibria predicted by the calculated isothermal section and contribute to the differences in the measured mechanical and electrical properties of the investigated alloys.

3.2. Mechanical properties

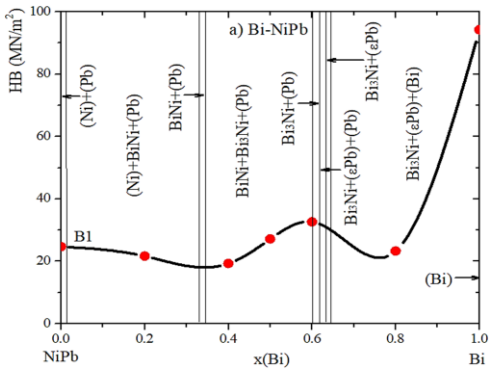
3.2.1. Experimental results

Brinell hardness measurements were performed at three different locations on each sample, and the results are summarised in Table 4. The table provides the sample identification numbers, the calculated phase fractions of the investigated alloys, the individual hardness values obtained from the three measurements and the corresponding average Brinell hardness values. For comparison, the hardness values of the pure constituent elements reported in the literature [22] are also included. The phase fractions of all investigated alloys at room temperature were determined using the thermodynamic database.

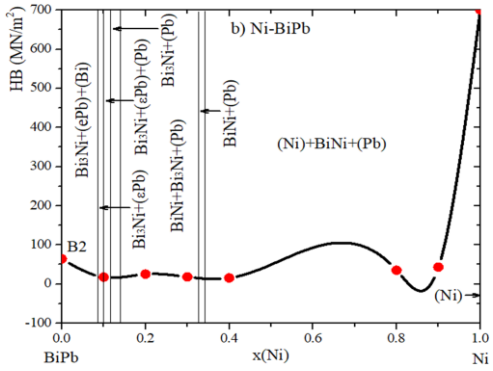
Figure 5 presents the mean Brinell hardness values listed in Table 4 as a function of alloy composition. The graphical representation provides a clear overview of the variation in hardness across the investigated composition ranges and facilitates the analysis of the relationship between alloy composition, phase constitution and the resulting mechanical response.

The measured Brinell hardness values show a clear dependence on the phase constitution of the investigated Bi-Ni-Pb alloys. As presented in Table 4 and Fig. 5, the hardness variation along the three investigated vertical sections is closely associated with changes in the relative fractions of the constituent phases. In particular, the results demonstrate that the mechanical response of the alloys cannot be described solely by their nominal chemical composition, but rather by the phase assemblage developed at room temperature.

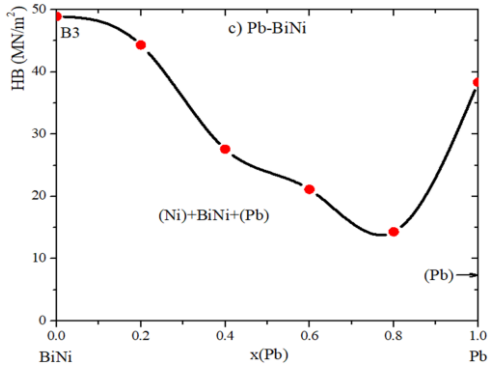
For the Bi-NiPb section (samples 1–5), the Brinell hardness values of the investigated alloys range from 19.3 to 32.6 MN/m^2. The observed variation in hardness can be associated with changes in the relative fractions of the constituent phases. Along this section, three different three-phase regions are encountered. Notably, samples 2–4 belong to the same three-phase region; however, their hardness values differ considerably, indicating that the hardness is influenced not only by the type of phases present but also by their relative proportions.



a).



b).



c).

Fig. 5. Graphical presentation of Brinell hardness dependence of composition and phase fraction: a) vertical section Bi-NiPb; b) vertical section Ni-BiPb; c) vertical section Pb-BiNi.

Sample 2 exhibits the lowest hardness among samples 2–4, with a value of 19.3 MN/m^2. Its phase constitution consists of approximately 17.9% Bi_3Ni, 51.3% BiNi and 30.8% (Pb). In sample 3, the fraction of Bi_3Ni increases substantially to approximately 48.4%, while the BiNi fraction decreases to 25.9%, and the (Pb) fraction remains approximately 25.7%. This change in phase fractions is accompanied by an increase in hardness to 27.1 MN/m^2. For sample 4, the Bi_3Ni fraction increases further to approximately 78.9%, while the fractions of the BiNi and (Pb) phases decrease considerably. Correspondingly, the hardness reaches 32.6 MN/m^2.

Table 4. Calculated phase fractions at room temperature and related Brinell hardness values of B1, B2, B3 and ternary Bi-Ni-Pb alloys.

Number	Calculated fraction of a phase (%)	Measured value (MN/m²)			Mean value (MN/m²)
		1	2	3	
B1	50.0 % (Pb), 50.0 % (Ni)	24.8	25.6	23.7	24.7
1	20.5 % (Ni), 39.1 % BiNi, 40.4 % (Pb)	20.1	22.5	22.3	21.63
2	17.9 % Bi_3Ni, 51.3 % BiNi, 30.8 % (Pb)	18.9	19.4	19.5	19.3
3	48.4 % Bi_3Ni, 25.9 % BiNi, 25.7 % (Pb)	25.5	26.2	29.6	27.1
4	78.9 % Bi_3Ni, 0.6 % BiNi, 20.5 % (Pb)	32.0	33.2	32.6	32.6
5	45.9 % (Bi), 40.0 % BiNi, 14.1 % (εPb)	20.4	24.4	25.1	23.3
Bi	100.0 % (Bi)				94.2 [22]
B2	70.4 % (εPb), 29.6 % (Bi)	64.1	62.8	65.7	64.2
6	40.0 % Bi_3Ni, 1.0 % (Pb), 59.0 % (εPb)	15.5	19.6	17.7	17.6
7	37.6 % Bi_3Ni, 21.3 % BiNi, 41.1 % (Pb)	23.5	26.6	25.4	25.2
8	7.6 % Bi_3Ni, 56.4 % BiNi, 36.0 % (Pb)	16.9	18.5	19.4	18.2
9	10.4 % (Ni), 30.3 % (Pb), 59.3 % BiNi	15.1	13.5	18.3	15.6
10	70.1 % (Ni), 10.1 % (Pb), 19.8 BiNi	34.1	35.1	35.7	34.9
11	85.1 % (Ni), 5.0 % (Pb), 9.9 % BiNi	49.8	52.7	57.1	53.2
Ni	100 % (Ni)				700 [22]
B3	99.9 % BiNi, 0.1 % (Ni)	50.8	47.1	48.9	48.9
12	79.5 % BiNi, 20.2 % (Pb), 0.3 % (Ni)	43.1	43.3	46.5	44.3
13	59.1 % BiNi, 40.4 % (Pb), 0.5 % (Ni)	27.0	28.1	27.7	27.6
14	38.8 % BiNi, 60.6 % (Pb), 0.6 % (Ni)	21.7	20.8	20.7	21.1
15	18.4 % BiNi, 80.8 % (Pb), 0.8 % (Ni)	14.0	14.7	14.3	14.3
Pb	100 % (Pb)				38.3 [22]

Table 5. Mixture model. Model summary statistics used for model selection.

Source	Std. dev.	R^2	Adjusted R^2	Predicted R^2	PRESS	
Linear	1.075535	0.228267	0.198003	0.134089	66.19505	
Quadratic	0.940062	0.445116	0.387316	0.249458	57.37556	
Special Cubic	0.71964	0.681598	0.640951	0.608051	29.96273	
Cubic	0.731591	0.684938	0.628926	0.587455	31.53719	Aliased
Special Quartic	0.698647	0.712674	0.661593	0.619531	29.08518	Suggested
Quartic	0.553781	0.831511	0.787382	0.774756	17.21889	Aliased

The progressive increase in hardness from sample 2 to sample 4 is therefore closely associated with the increasing fraction of the Bi_3Ni phase and the simultaneous reduction in the fractions of the BiNi and Pb-rich constituents. The Bi_3Ni frac-tion increases from 17.9% in sample 2 to 48.4% in sample 3 and 78.9% in sample 4, accompanied by an increase in hardness of approximately 41% and 69%, respectively, relative to sample 2. This trend suggests that Bi_3Ni makes a significant contribution to the overall hardness of the alloys, while the decreasing fraction of the softer Pb-rich constituent further promotes the increase in hardness. These results demonstrate that, even within the same three-phase region, changes in the relative phase fractions can produce a pronounced variation in Brinell hardness.

For the Ni-BiPb section represented by samples 6–11, the Brinell hardness values show a pronounced variation with alloy composition and phase constitution. The investigated compositions are located within three different three-phase regions, indicating that changes in hardness are associated both with changes in the phase assemblage and with variations in the relative fractions of the individual phases.

A more detailed comparison can be made for samples 9–11, which belong to the same three-phase region. Despite having the same type of three-phase phase assemblage, these samples exhibit significant differences in Brinell hardness, demonstrating that the mechanical response is strongly affected by the relative phase fractions. The hardness increases progressively toward sample 11, reaching the highest value of 53.2 MN/m^2. This increase can be associated with the changing proportions of the constituent phases, particularly the increasing fraction of the harder Ni-rich phase (Ni) and the corresponding reduction in the softer constituents.

The comparison of samples 9–11 is particularly important because the phase assemblage remains unchanged, while the phase fractions vary with composition. Therefore, the observed change in hardness cannot be attributed to the appearance of a new phase, but rather to the changing relative contribution of the phases already present. The higher hardness observed for

sample 11 indicates that its phase constitution is more favourable for strengthening, with the larger fraction of the Ni-rich constituent contributing significantly to the overall mechanical response. Conversely, the lower hardness of samples 9 and 10 can be related to their higher proportions of the softer constituents.

Overall, the results for samples 6–11 demonstrate that Brinell hardness is governed by both the type of three-phase region and, importantly, the relative fractions of the constituent phases. The comparison of samples 9–11 shows that substantial changes in hardness can occur even within the same three-phase region, highlighting the significant influence of phase fraction on the mechanical properties of the investigated alloys.

For samples 12–15, all compositions belong to the same three-phase region, allowing the effect of changing phase fractions on Brinell hardness to be evaluated without a change in the phase assemblage. The hardness decreases progressively from 44.3 MN/m^2 for sample 12 to 14.3 MN/m^2 for sample 15. This decrease is associated with a reduction in the fraction of the harder Bi_3Ni phase, from approximately 79.5% in sample 12 to 18.4% in sample 15, accompanied by an increase in the Pb-rich constituent to approximately 80.8%. The results therefore indicate that, even within the same three-phase region, variations in the relative phase fractions have a pronounced effect on hardness, with a higher Bi_3Ni fraction contributing to increased hardness, while an increasing Pb-rich fraction promotes softening.

Among all investigated alloys, the highest Brinell hardness value was recorded for sample 11, reaching 53.2 MN/m^2. The lowest Brinell hardness value was determined for sample 15.

The experimental data given in Table 4 were further used to develop a mathematical model for predicting Brinell hardness across the entire composition range.

3.2.2. Development and validation of the mixture model for Brinell hardness

The hardness model was developed using all experimentally measured Brinell hardness values obtained for the investigated alloy compositions. Three independent hardness measurements were performed for each of the eighteen alloy compositions, resulting in a total of fifty-four experimental observations. In contrast to the previous preliminary analysis based on composition averages, all individual measurements were retained in the regression analysis in order to provide an unbiased estimate of the experimental (pure) error and to enable a statistically valid lack-of-fit test.

Model selection

To describe the influence of the Bi-Ni-Pb composition on Brinell hardness (HB), several Scheffé mixture models of increasing complexity (linear, quadratic, special cubic and special quartic) were evaluated using Design-Expert® software. Model selection was based on standard statistical criteria including the determination (R^2), adjusted coefficient of determination (Adj. R^2), predicted coefficient of determination (Pred. R^2), prediction error sum of squares (PRESS) and adequate precision. In accordance with the principle of parsimony, the simplest hierarchical model providing satisfactory predictive performance was selected (Table 5).

The special cubic mixture model was selected because it provides an adequate balance between goodness of fit and model simplicity. Although the special quartic model produced slightly lower residual error and slightly higher coefficients of determination, the improvement was relatively small, while requiring additional higher-order interaction terms. Since the objective was to obtain a statistically sound and physically interpretable model, the hierarchical special cubic model was adopted for subsequent analyses.

Analysis of variance

The analysis of variance (ANOVA) for the selected special cubic model is presented in Table 6. The overall regression model was highly significant ($F = 16.77$, $p < 0.0001$), indicating that the selected polynomial adequately describes the relationship between alloy composition and Brinell hardness. Among the regression terms, the Bi-Ni (AB), Bi-Pb (AC) and ternary interaction (ABC) were statistically significant ($p < 0.05$), whereas the Ni-Pb interaction (BC) was not statistically significant (Table 7).

The obtained coefficient of determination ($R^2 = 0.682$) indicates that approximately 68% of the total variation in hardness is explained by the selected model. The adjusted coefficient of determination (Adj. $R^2 = 0.641$) remained close to R^2, indicat-

Table 6. ANOVA for special cubic mixture model.

Source	Sum of squares	Degrees of freedom	Mean square	F-value	p-value Prob > F	
Model	52.10509	6	8.684182	16.76866	3.15E–10	significant
Linear mixture	17.44998	2	8.724992	16.84747	3.04E–06	
AB	4.607531	1	4.607531	8.896881	0.004518	
AC	14.32134	1	14.32134	27.6537	3.49E–06	
BC	0.16212	1	0.16212	0.313045	0.578474	
ABC	18.07794	1	18.07794	34.90747	3.7E–07	
Residual	24.34043	47	0.517882			
Lack of fit	23.39639	11	2.126944	81.10836	5.33E–22	significant
Pure error	0.944046	36	0.026223			
Corrected total	76.44552	53				

Table 7. Summary statistics for the selected special cubic mixture model.

Std. dev.	0.71964	**R-squared**	0.681598
Mean	5.314471	**Adj. R-squared**	0.640951
Coeff. var. %	13.54114	**Pred. R-squared**	0.608051
PRESS	29.96273	**Adeq. Precision**	13.32147

ing that unnecessary model terms were not introduced. Likewise, the predicted coefficient of determination (Pred. R^2 = 0.608) differed from Adj. R^2 by less than 0.2, indicating moderate but acceptable predictive capability within the investigated experimental domain. The Adeq. Precision ratio reached 13.32, which is considerably higher than the recommended minimum value of 4, indicating an adequate signal-to-noise ratio for navigation throughout the investigated composition space. The residual standard deviation (std. dev. = 0.720) and PRESS value (29.96) provide additional measures of the model prediction error and should be considered together with the moderate Pred. R^2 value when assessing its predictive performance.

Although the lack-of-fit test was statistically significant, this result is primarily attributed to the very small pure experimental error obtained from the replicated measurements, which makes residual standard deviation, coefficient of determination and the lack-of-fit test highly sensitive even to relatively small deviations between the fitted model and the experimental data. Nevertheless, the residual diagnostic plots showed no systematic patterns or violations of the underlying regression assumptions, while the model retained acceptable predictive capability (Pred. R^2 = 0.608). Therefore, the model was considered adequate for describing the overall compositional trends within the investigated experimental domain, although its predictive accuracy should be regarded as moderate rather than high.

Regression equation and interpretation of the transformed response

The final regression equation describing the square-root transformed Brinell hardness is:

$$(HB)^{0.5}=3.002415(Bi) + 6.917359(Ni) + 2.143854(Pb) + 9.336419(Bi)(Ni) + 18.39945(Bi)(Pb) + \\ + 1.751249(Ni)(Pb) - 71.2602(Bi)(Ni)(Pb). \quad (7)$$

where Bi, Ni and Pb denote the corresponding component fractions in the alloy. The component fractions are expressed in mass fraction and satisfy Bi+Ni+Pb=1.

The linear coefficients do not represent the hardness of the pure components. Instead, they correspond to the linear contribution of each component within the constrained Scheffé mixture model and should therefore be interpreted only together with the interaction terms.

The positive coefficients associated with the Bi-Ni and Bi-Pb interactions indicate positive interaction effects on the square-root transformed hardness response, which are reflected in increased predicted hardness in the corresponding compositional regions after back-transformation, whereas the large negative coefficient of the ternary interaction suggests that the simultaneous presence of all three components reduces hardness relative to that expected from the binary interactions alone.

For practical application, the predicted Brinell hardness is obtained by applying the inverse transformation,

$$HB=[(HB)^{0.5}]^2. \quad (8)$$

Accordingly, the regression equation is first used to calculate the transformed response, after which the predicted Brinell hardness is obtained by squaring the calculated value.

Model diagnostics

Figure 6 shows the diagnostic plots used to validate the regression model. The normal probability plot confirms approximate normality of residuals. Residuals are randomly distributed around zero without systematic trends, indicating homoscedasticity. No influential observations were detected based on externally studentised residuals and Cook's distance. None of the observations exceeded the commonly accepted influence limits. Likewise, the residuals showed no dependence on experimental run order, confirming statistical independence of the observations.

The Box-Cox analysis suggested an optimum transformation close to λ = –0.1. However, the square-root transformation (λ = 0.5) was retained because it lies within the 95% confidence interval of acceptable transformations while providing a simpler and more physically interpretable response transformation. The selected transformation also resulted in satisfactory residual diagnostics and stable prediction performance (Fig. 7).

Response surface analysis

The predicted variation of Brinell hardness throughout the investigated Bi-Ni-Pb composition space is illustrated in Fig. 8.

The contour plot reveals a distinctly nonlinear response surface, indicating pronounced interaction effects among the alloying elements. The highest predicted hardness values are observed in the Bi-Ni-rich region with moderate Pb content, whereas increasing Pb content generally leads to lower hardness. The curvature of the contour lines reflects the contribution of the binary Bi-Ni and Bi-Pb interactions as well as the ternary Bi-Ni-Pb interaction included in the selected special cubic model. This behaviour is consistent with the regression analysis, particularly with the positive Bi-Ni interaction and the negative ternary interaction.

Although the regression analysis was performed using the transformed response, all graphical presentations of the response surface and all reported optimum hardness values are expressed on the original Brinell hardness scale after back-transformation, thereby facilitating engineering interpretation of the results.

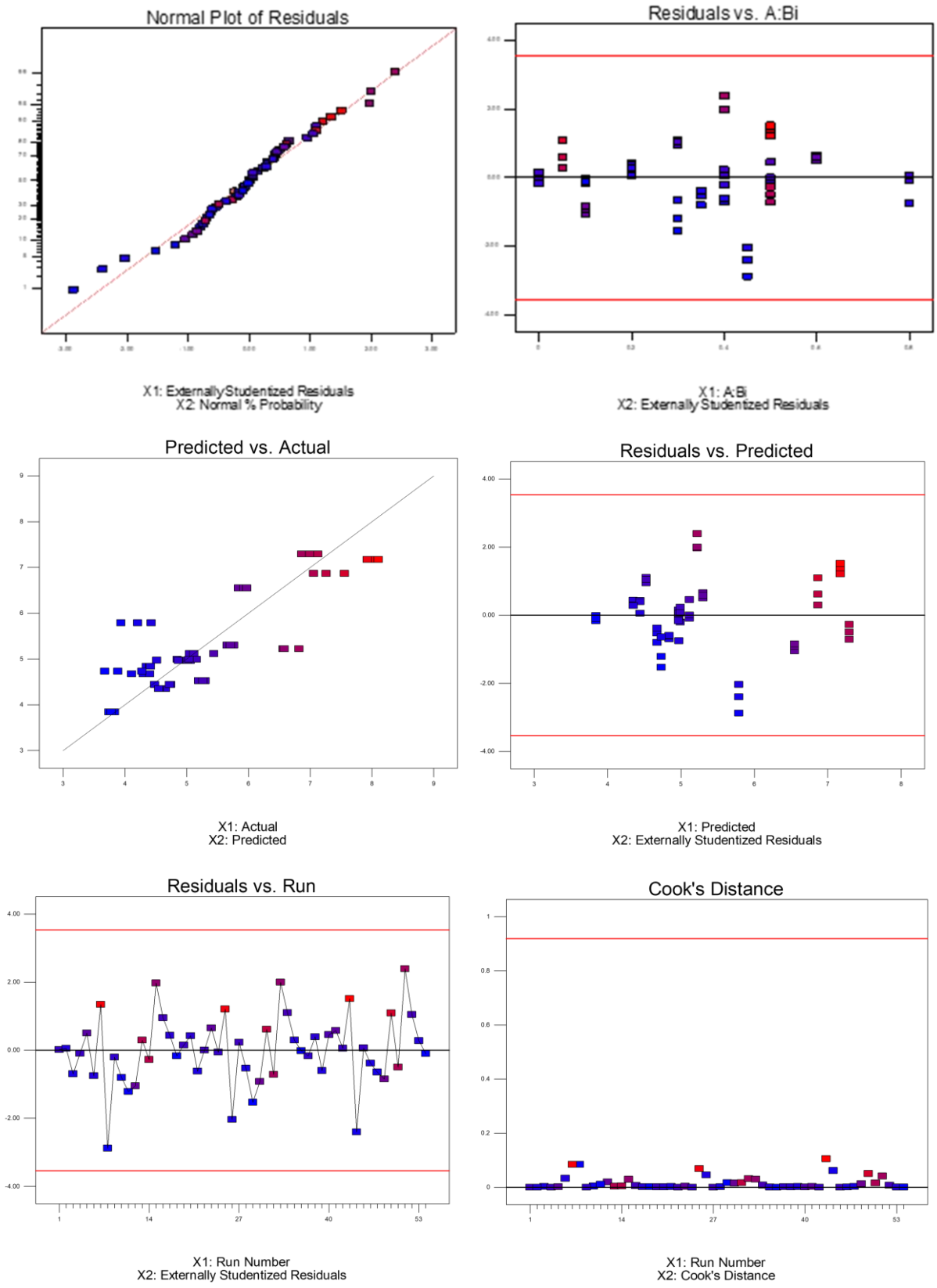


Fig. 6. Diagnostic plots used to evaluate the adequacy of the Brinell hardness regression model.

Based on the statistical evaluation, diagnostic analysis and predictive performance, the special cubic Scheffé mixture model with square-root transformation was selected as the final mathematical model for describing the influence of Bi-Ni-Pb composition on Brinell hardness. Although more complex quartic models yielded only marginal improvements in goodness-of-fit sta-

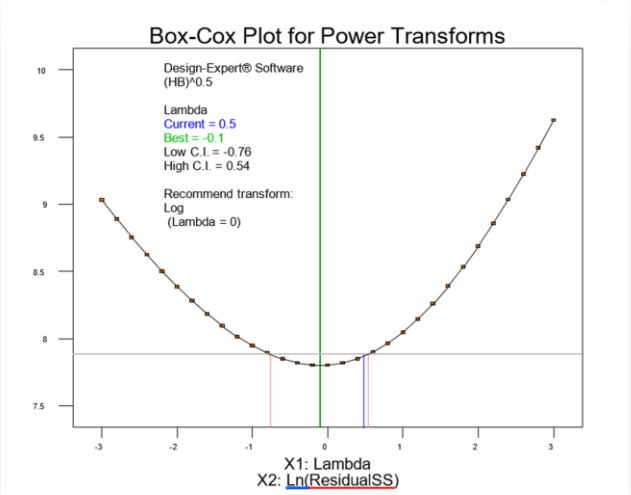


Fig. 7. Box–Cox plot for the Brinell hardness response showing the selected square-root transformation ($\lambda = 0.5$).

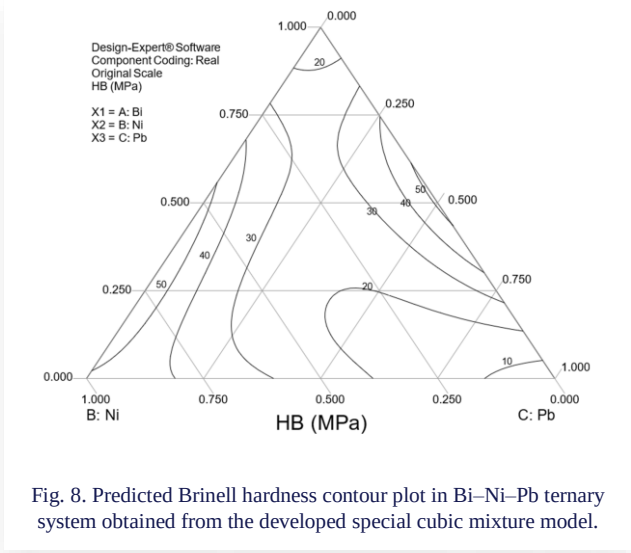


Fig. 8. Predicted Brinell hardness contour plot in Bi–Ni–Pb ternary system obtained from the developed special cubic mixture model.

tistics, they introduced additional higher-order interaction terms without substantially improving predictive capability. Therefore, the selected special cubic model represents the most appropriate compromise between statistical quality, physical interpretability and model simplicity for describing compositional trends and graphical analysis within the investigated experimental domain.

Confirmation of model predictions

The predictive performance of the developed special cubic Scheffé model was further evaluated by confirmation experiments at three selected compositions within the investigated composition space. For each confirmation point, Brinell hardness was measured at three different locations, and the arithmetic mean of the three measurements was used as the observed response. The experimental mean values were compared with the corresponding model predictions and the 95% prediction intervals, as summarised in Table 8.

Good agreement between the experimental and predicted responses was obtained for the first two confirmation points. At point 1, the experimentally determined mean hardness was 21.733 HB compared with the predicted value of 20.264 HB, while at point 2 the experimental and predicted values were 25.167 and 25.152 HB, respectively. A larger deviation was observed at point 3, where the experimental mean hardness (35.267 HB) exceeded the predicted value (27.790 HB). Nevertheless, the experimental mean values for all three confir-mation points were within their corresponding 95% prediction intervals. These results confirm that the developed model pro-vides an acceptable representation of Brinell hardness within the investigated composition domain, while the larger deviation ob-served at point 3 indicates locally increased uncertainty in model prediction.

The larger deviation observed at point 3 may be associated with increased local microstructural heterogeneity and variations in phase distribution at this composition. Since Brinell hardness is sensitive to the local microstructure within the indentation region, such heterogeneity may contribute to greater experimental variability and consequently to the observed difference between the experimental and predicted mean value.

Table 8. Results of confirmation experiments for the developed Brinell hardness model.

Point	Bi	Ni	Pb	Observed mean (HB)	Predicted mean (HB)	95% prediction interval	Validation
1	0.20	0.40	0.40	21.733	20.264	12.536–28.588	Confirmed
2	0.40	0.20	0.40	25.167	25.152	16.864–34.558	Confirmed
3	0.40	0.40	0.20	35.267	27.790	18.686–37.475	Confirmed

3.3. Electrical properties

3.3.1. Experimental results

Electrical conductivity measurements were performed on the samples listed in Table 1. For each sample, four measurements of electrical conductivity were carried out, and the results are presented in Table 9 and Fig. 9.

In addition to the experimental values, Table 9 also includes the calculated phase fractions, the mean values obtained from the four measurements and literature values of electrical conductivity for the pure elements [25].

The measured electrical conductivity of the investigated Bi-Ni-Pb alloys show a pronounced dependence on phase composition and phase fraction. The results indicate that the electrical transport properties cannot be described solely in terms of the nominal elemental composition, since the formation of intermetallic phases significantly modifies the conductivity of the alloys. This is particularly evident when comparing the conduc-

tivity of the individual constituents with that of the multiphase samples. The reference values are approximately 14.0 MS/m for (Ni), 4.8 MS/m for (Pb), and 0.77 MS/m for (Bi), whereas most of the multiphase alloys exhibit substantially lower conductivities.

The alloys containing a high fraction of Ni-rich phases (Ni), generally show the highest electrical conductivity among the investigated multiphase compositions. For example, samples 10 and 11, containing 70.1% and 85.1% (Ni), respectively, together with BiNi and Pb-containing (Pb) phases, exhibit conductivities of 5.5260 and 6.1861 MS/m. The relatively high conductivity of these samples can be attributed to the dominant contribution of the Ni-rich constituent, which provides comparatively efficient electron transport. Nevertheless, their conductivity remains considerably lower than that of pure Ni, indicating that the presence of Bi-containing and intermetallic phases introduces additional scattering and interrupts the continuous conductive Ni-rich paths.

A markedly different behaviour is observed for compositions dominated by BiNi and other Bi-Ni intermetallic phases. The reference sample B3, consisting of 99.9% BiNi, exhibits a conductivity of 2.108 MS/m, which is substantially lower than that of pure Ni and Pb. Furthermore, samples 12–15, in which the BiNi phase is combined predominantly with Pb, show conductivities ranging from 0.4169 to 2.7025 MS/m. An increase in the Pb fraction from 20.2% to 80.8% is accompanied by a general increase in conductivity. This trend suggests that, despite the relatively high intrinsic conductivity of Pb compared with BiNi, the overall electrical response is strongly influenced by the connectivity and spatial distribution of the phases. Increasing the Pb fraction may promote the formation of more continuous Pb-rich conductive regions.

The lowest conductivities are generally observed in alloys containing substantial fractions of Bi-rich and Bi-Ni inter-metallic phases. Samples 1–5 and 7–8 exhibit conductivities between approximately 0.47 and 0.96 MS/m, despite considerable differences in their phase fractions. For instance, sample 5, containing 45.9% (Bi), 40.0% BiNi and 14.1% (εPb), has a conductivity of only 0.4742 MS/m. Similarly, sample 2, containing 17.9% Bi_3Ni, 51.3% BiNi and 30.8% Pb, exhibits a conductivity of 0.5918 MS/m. These results demonstrate that a high proportion of Bi-rich or Bi-Ni intermetallic phases can strongly suppress electrical transport. The relatively low conductivity of Bi compared with Pb and Ni, combined with the intrinsically lower conductivity of the intermetallic phases, is likely responsible for this behaviour.

The comparison of samples 6–9 further demonstrates the importance of phase connectivity. Sample 6, containing 59.0% (εPb) and 40.0% Bi_3Ni, exhibits a conductivity of 1.2167 MS/m, while sample 9, with a high fraction of BiNi (59.3%) and a lower Bi fraction, reaches 1.6670 MS/m. Thus, the conductivity does not follow a simple linear relationship with the fraction of any single phase. Instead, it reflects the combined effects of phase fraction, intrinsic conductivity, interfacial scattering, and the continuity of electrically conductive paths through the microstructure.

The binary Pb-Ni alloy B1, containing 50% (Pb) and 50% (Ni), exhibits a conductivity of 3.1862 MS/m, which is

Table 9. Calculated phase fractions at room temperature and related electrical conductivity values of B1, B2, B3 and ternary Bi-Ni-Pb alloys.

Number	Calculated fraction of a phase (%)	Measured value (MS/m)				Mean value (MS/m)
		1	2	3	4	
B1	50.0% (Pb), 50.0% (Ni)	3.1876	3.1872	3.1845	3.1856	3.1862
1	20.5 % (Ni), 39.1 % BiNi, 40.4 % (Pb)	0.8726	0.8706	0.8614	0.8648	0.8673
2	17.9 % Bi_3Ni, 51.3 % BiNi, 30.8 % (Pb)	0.5869	0.5876	0.5963	0.5964	0.5918
3	48.4 % Bi_3Ni, 25.9 % BiNi, 25.7 % (Pb)	0.6536	0.6502	0.6635	0.6630	0.6575
4	78.9 % Bi_3Ni, 0.6 % BiNi, 20.5 % (Pb)	0.6816	0.6762	0.6796	0.6794	0.6792
5	45.9 % (Bi), 40.0 % BiNi, 14.1 % (εPb)	0.4737	0.4751	0.4769	0.4711	0.4742
Bi	100.0 % (Bi)					0.77 [23]
B2	70.4 % (εPb), 29.6 % (Bi)	0.5532	0.5454	0.5563	0.5481	0.5507
6	40.0 % Bi_3Ni, 1.0 % (Pb), 59.0 % (εPb)	1.2230	1.2100	1.2200	1.2140	1.2167
7	37.6 % Bi_3Ni, 21.3 % BiNi, 41.1 % (Pb)	0.9635	0.9621	0.9646	0.9643	0.9636
8	7.6 % Bi_3Ni, 56.4 % BiNI, 36.0 % (Pb)	0.6105	0.6082	0.6188	0.6089	0.6116
9	10.4 % (Ni), 30.3 % (Pb), 59.3 % BiNi	1.6687	1.6661	1.6690	1.6643	1.6670
10	70.1 % (Ni), 10.1 % (Pb), 19.8 % BiNi	5.5249	5.5251	5.5293	5.5250	5.5260
11	85.1 % (Ni), 5.0 % (Pb), 9.9 % BiNi	6.1873	6.1832	6.1843	6.1898	6.1861
Ni	100 % (Ni)					14.0 [23]
B3	99.9 % BiNi, 0.1 % (Ni)	2.1090	2.1078	2.1098	2.1068	2.108
12	79.5 % BiNi, 20.2 % (Pb), 0.3 % (Ni)	0.3871	0.4765	0.3986	0.4056	0.4169
13	59.1 % BiNi, 40.4 % (Pb), 0.5 % (Ni)	0.7950	0.7947	0.7963	0.7930	0.7947
14	38.8 % BiNi, 60.6 % (Pb), 0.6 % (Ni)	1.3860	1.3900	1.3820	1.3760	1.3835
15	18.4 % BiNi, 80.8 % (Pb), 0.8 % (Ni)	2.6970	2.7200	2.6950	2.6980	2.7025
Pb	100 % (Pb)					4.8 [23]

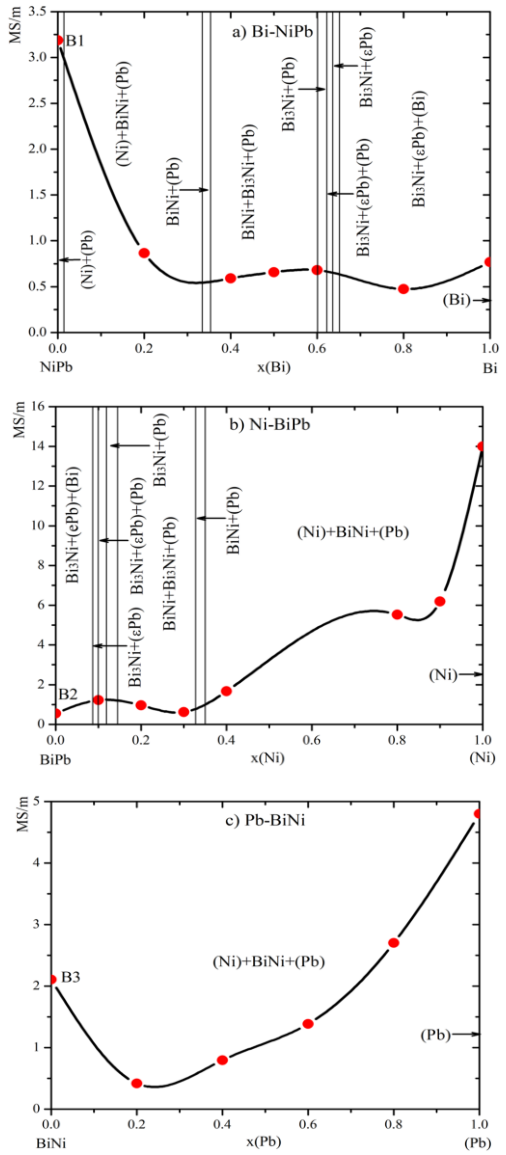


Fig. 9. Graphical presentation of electrical conductivity dependence of composition and phase fraction: a) vertical section Bi-NiPb; b) vertical section Ni-BiPb; c) vertical section Pb-BiNi.

considerably lower than would be expected from the conductivity of the pure constituents based solely on their volume fractions. This reduction can be associated with the formation of additional phases and with the disruption of continuous metallic conduction paths. Consequently, the experimental results confirm that phase transformations and intermetallic-phase formation play a crucial role in determining the electrical properties of the investigated alloys.

Overall, the results demonstrate that increasing the fraction of highly conductive Ni-rich regions tends to increase electrical conductivity, whereas increasing the proportion of Bi-rich and Bi-Ni intermetallic phases generally lead to lower conductivity. The results show that sample 11 exhibits the highest electrical conductivity among all investigated ternary alloys. This is attributed to the high fraction of the (Ni) solid solution in the alloy (85.1%), while the remaining phases are 9.9% BiNi and 5.0% (Pb).

Figure 9 presents a graphical representation of the mean values given in Table 9, providing a clearer overview of the results.

3.3.2. Response surface model for electrical conductivity

Model selection

The relationship between the chemical composition of the Bi-Ni-Pb alloys and electrical conductivity (EP) was analysed using a quadratic Scheffé mixture model. The model was selected based on the sequential model sum of squares, statistical significance of the regression terms, model hierarchy and predictive capability. Although higher-order models slightly improved the coefficient of determination, they were either aliased or non-hierarchical and therefore unsuitable for practical application. Consequently, the quadratic model was selected as the most appropriate compromise between statistical performance, interpretability and predictive capability.

Model development using alloy compositions

The experimental values corresponding to the pure components (100 wt.% Bi, 100 wt.% Ni and 100 wt.% Pb) were excluded from the regression analysis used to construct the response surface model. These compositions represent the vertices of the simplex and exhibit electrical conductivity values that differ markedly from those of the investigated ternary alloys.

Their inclusion produced pronounced leverage effects, resulting in poor regression diagnostics and a statistically significant lack of fit. Consequently, these extreme compositions prevented the construction of a predictive response surface representative of the investigated alloy system.

Since the objective of the mixture design was to model the electrical conductivity within the practical composition region of the Bi-Ni-Pb alloys rather than the pure constituents, the regression model was developed using only the alloy compositions.

Preliminary analyses performed with all experimental points included produced substantially poorer diagnostic statistics and pronounced systematic deviations in the residual plots, indicating that the extreme responses of the pure components dominated the regression. Therefore, these points were omitted from the final model.

Model summary statistics

The statistical indicators summarised in Table 10 demonstrate that the selected quadratic Scheffé model provides a good balance between goodness of fit, predictive capability and model robustness.

ANOVA

The ANOVA results confirmed that the developed model was highly significant ($p < 0.0001$). The coefficient of determination was $R^2 = 0.9522$, indicating that more than 95% of the variability in electrical conductivity was explained by the alloy composition. The adjusted and predicted coefficients of determination were Adj. $R^2 = 0.9486$ and Pred. $R^2 = 0.9451$, respectively, demonstrating excellent agreement between model fitting and

Table 10. Model summary statistics used for selection of the quadratic Scheffé mixture model.

Statistic	Value	Interpretation
R^2	0.9522	Excellent model fit; 95.22% of the variability explained
Adjusted R^2	0.9486	High explanatory capability after accounting for model complexity
Predicted R^2	0.9451	High predictive capability for new observations
Std. dev.	0.3787	Low residual variability around the fitted model
PRESS	10.883	Low prediction error, indicating robust model performance
Adeq. Precision	55.89	Far above the recommended value of 4, indicating an excellent signal-to-noise ratio

predictive performance. Furthermore, the Adeq. Precision ratio of 55.89 was substantially higher than the recommended minimum value of 4, indicating an adequate signal-to-noise ratio and confirming that the model can be reliably used to navigate the design space.

The significance of the individual model terms is summarised in Table 11. All linear mixture components and binary interaction terms were statistically significant ($p < 0.0001$), indicating that both the individual alloy constituents and their interactions significantly affected electrical conductivity. Among the interaction terms, the Ni-Pb interaction exhibited the largest F-value, indicating that this binary interaction had the strongest influence on electrical conductivity.

Table 11. ANOVA for the quadratic Scheffé mixture model of electrical conductivity.

Source	Sum of squares	df	Mean square	F-value	p-value
Model	188.7243	5	37.7449	263.20	<0.0001
Linear mixture	142.8060	2	71.4030	497.90	<0.0001
AB	16.8962	1	16.8962	117.82	<0.0001
AC	7.8048	1	7.8048	54.42	<0.0001
BC	24.3914	1	24.3914	170.08	<0.0001
Residual	9.4650	66	0.1434		
Lack of fit	9.4589	12	0.7882	7004.36	<0.0001
Pure error	0.0061	54	0.0001		

Regression equation

The final quadratic Scheffé mixture equation describing the dependence of electrical conductivity on alloy composition is expressed as:

$$EP = 1.4588(\mathrm{Bi}) + 8.2429(\mathrm{Ni}) + 4.6059(\mathrm{Pb}) + \\ - 11.7571(\mathrm{Bi})(\mathrm{Ni}) - 8.7015(\mathrm{Bi})(\mathrm{Pb}) - 14.1497(\mathrm{Ni})(\mathrm{Pb}) \quad (9)$$

where Bi, Ni and Pb denote the mass fractions of the corresponding alloy components.

Interpretation of coefficients

Among the linear blending coefficients, Ni has the largest positive coefficient, indicating that increasing the relative contribution of Ni is associated with higher electrical conductivity within the investigated mixture domain. Pb exhibits an intermediate contribution, whereas Bi has the lowest linear blending coefficient. The negative interaction coefficients for Bi-Ni, Bi-Pb, and Ni-Pb indicate antagonistic deviations from linear blending, meaning that the conductivity of the corresponding binary mixtures is lower than would be expected from the linear contributions of the individual components.

The magnitude of the interaction coefficients indicates that the Ni-Pb interaction exerts the strongest negative influence on electrical conductivity, followed by the Bi-Ni and Bi-Pb interactions. This suggests that the electrical conductivity cannot be predicted by a simple rule of mixtures but is strongly affected by interactions among the alloy constituents.

Diagnostic plots

Diagnostic plots of the selected model are presented in Fig. 10. The normal probability plot of residuals showed an approximately linear distribution, indicating that the residuals were close to normally distributed. The residuals versus predicted values plot revealed no systematic pattern, confirming homoscedasticity of the residuals. Likewise, the residuals plotted against the experimental run order showed random scatter, suggesting the absence of time-dependent effects or systematic experimental errors. The predicted versus actual values exhibited excellent agreement, confirming the high predictive capability of the developed model.

Finally, the Box-Cox analysis indicated that the original response scale was appropriate, as the current transformation parameter ($\lambda = 1$) lay within the confidence interval around the optimum value in Fig. 11.

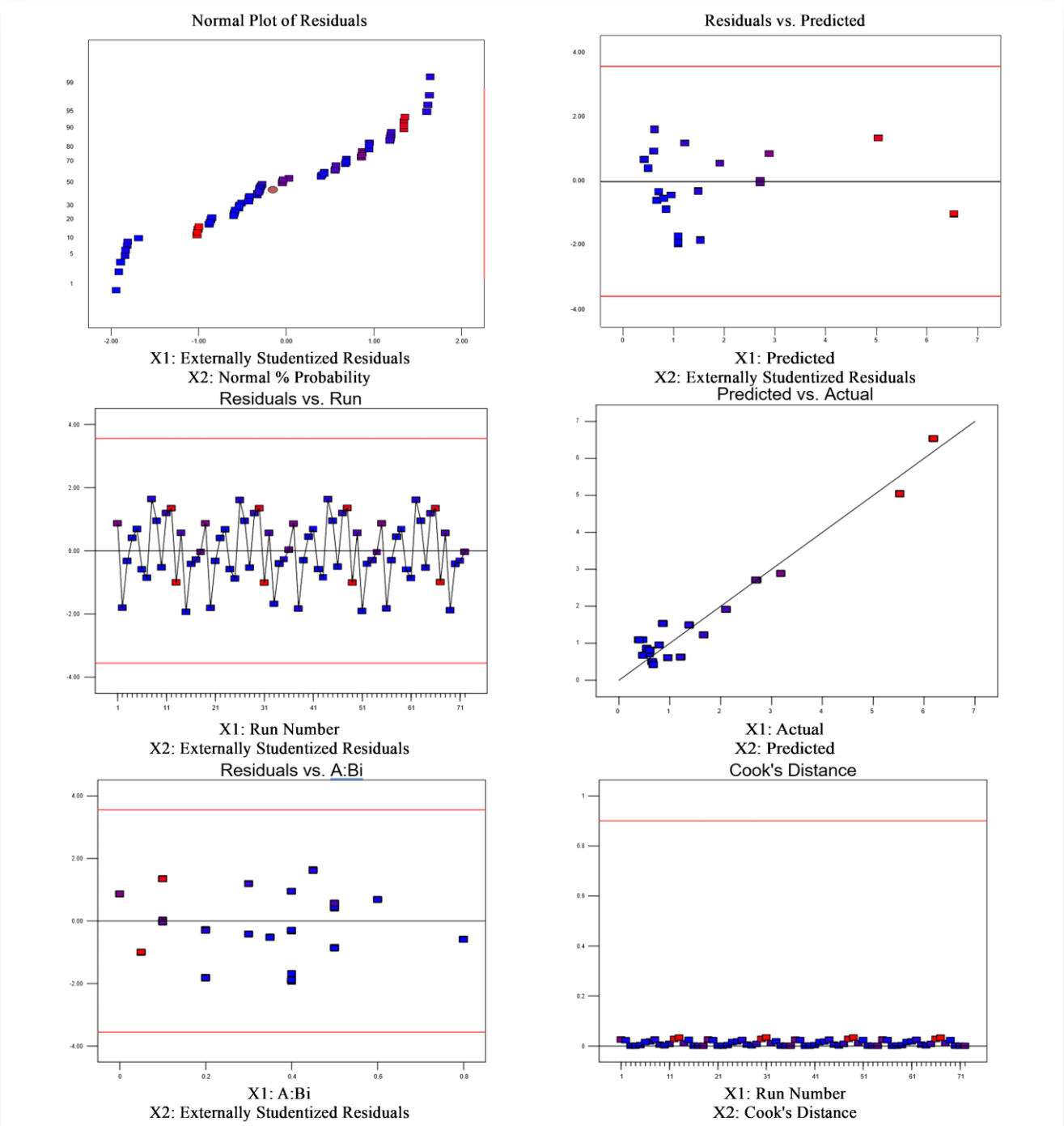


Fig. 10. Diagnostic plots for the selected quadratic Scheffé mixture model of electrical conductivity.

Although the lack-of-fit test was statistically significant, the pure experimental error was exceptionally low because of the excellent repeatability of the electrical conductivity measurements. Consequently, the lack-of-fit test became highly sensitive, such that even relatively small deviations between the fitted model and the experimental observations resulted in a statistically significant lack-of-fit. Nevertheless, the diagnostic plots revealed no systematic deviations, and the model exhibited excellent predictive capability (Pred. R^2 = 0.9451). Therefore, the quadratic model was considered adequate for prediction within the investigated experimental domain. Overall, these diagnostic results demonstrate that the quadratic Scheffé mixture model provides an adequate and statistically reliable description of the relationship between alloy composition and electrical conductivity within the investigated experimental region.

Contour plot

The contour plot generated from the quadratic Scheffé mixture model is presented in Fig. 12. This graphical representation illustrates the combined influence of Bi, Ni and Pb contents on

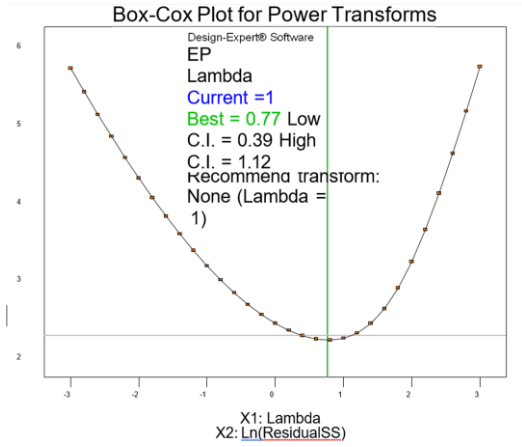


Fig. 11. Box–Cox plot for the electrical conductivity response.

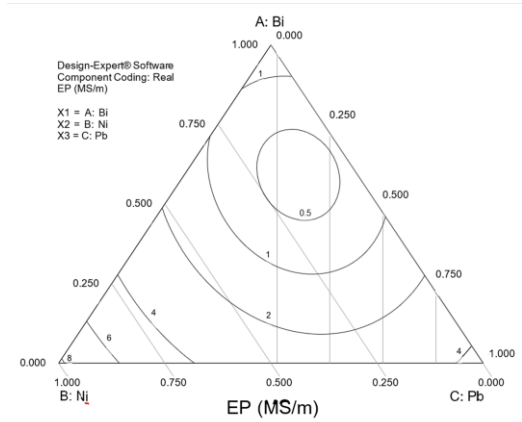


Fig. 12. Predicted electrical conductivity contour plot in the Bi-Ni-Pb ternary system obtained from the developed quadratic Scheffé mixture model.

the electrical conductivity of the investigated alloys and provides a clear visualisation of the predicted response throughout the composition domain.

The contour plot reveals a pronounced compositional dependence of electrical conductivity. The highest conductivity values are predicted in the Ni-rich region of the ternary diagram, where the nickel content approaches its upper limit within the investigated experimental domain. In contrast, conductivity decreases markedly with the increasing Bi content, reaching its minimum in the Bi-rich corner of the composition triangle. Alloys containing intermediate amounts of Pb exhibit conductivity values between these two extremes, indicating that the influence of Pb is less pronounced than that of Ni but considerably more favourable than that of Bi.

The curved contour lines demonstrate that the relationship between alloy composition and electrical conductivity is nonlinear. The absence of abrupt changes in the contour pattern indicates that the developed quadratic model provides a smooth description of the composition–property relationship within the investigated domain. Instead of varying according to a simple linear mixing rule, conductivity changes progressively across the composition triangle, reflecting significant interactions among the alloying elements. This behaviour is consistent with the significant interaction terms (Bi×Ni, Bi×Pb and Ni×Pb) identified in the quadratic mixture model. The negative interaction coefficients indicate that simultaneous increases in two components reduce the conductivity relative to the value expected from their individual linear contributions.

Overall, the contour plot demonstrates that nickel is the dominant component associated with higher electrical conductivity in the Bi-Ni-Pb system, whereas increasing bismuth content is associated with lower conductivity. Lead exhibits an intermediate effect, while the curvature of the contour lines reflects the significant binary interactions identified by the quadratic Scheffé mixture model. The graphical analysis therefore supports the compositional trends identified by the statistical evaluation of the model.

Confirmation of model predictions

To verify the predictive capability of the developed quadratic Scheffé mixture model, three additional binary alloy compositions that were not included in the model fitting procedure were experimentally prepared and tested. The investigated compositions were Bi-Ni (0.5-0.5-0), Bi-Pb (0.5-0-0.5) and Ni-Pb (0-0.5-0.5). For each composition, electrical conductivity was measured four times, and the average value was calculated.

Table 12 compares the experimentally measured electrical conductivity values with those predicted by the quadratic mixture model. The measured average electrical conductivities were 2.1045, 0.6982 and 3.1158 MS/m for the Bi-Ni, Bi-Pb and Ni-Pb alloys, respectively, whereas the corresponding model predictions were 1.9116, 0.8570 and 2.8870 MS/m.

Although small differences between the predicted and experimental values were observed, all measured values were located within the corresponding 95% prediction intervals generated by the model. This indicates that the deviations are within the expected prediction uncertainty and confirms the satisfactory predictive capability of the developed quadratic mixture model.

The confirmation experiments therefore demonstrate that the quadratic Scheffé model reliably predicts the electrical conductivity of Bi-Ni-Pb alloys within the investigated composition region and can therefore be confidently used for interpolation and alloy composition optimization within this domain.

Table 12. Results of confirmation experiments for the developed electrical conductivity model.

Composition (Bi-Ni-Pb)	Predicted (MS/m)	Experimental (MS/m)	95% Prediction interval (MS/m)	Validation
0.5-0.5-0.0	1.9116	2.1045	1.4257–2.3975	within PI
0.5-0.0-0.5	0.8570	0.6982	0.3949–1.3191	within PI
0.0-0.5-0.5	2.8870	3.1158	2.3995–3.3745	within PI

3.4. Scheil and Lever solidification simulations

Sample 11, $Bi_5Ni_{90}Pb_5$, exhibited a favourable combination of both hardness and electrical conductivity among all investigated ternary alloys. This sample was selected for solidification simulations. The simulations were performed using Scheil and Lever models, and the results are presented in Fig. 13.

The non-equilibrium (Scheil) simulation is shown as a blue curve, while the equilibrium (Lever) simulation is represented by a red curve. During non-equilibrium solidification, seven phases are predicted to form, whereas five phases are formed under equilibrium conditions.

Figure 14 presents the calculated solidification behaviour of the $Bi_5Ni_{90}Pb_5$ alloy using the Scheil and Lever models. Both simulations predict a very similar overall solidification sequence, indicating that the alloy solidifies predominantly through the formation of a Ni-rich solid solution (Ni), followed by the appearance of Bi-Ni intermetallic phases and, at lower temperatures, Pb-rich and Bi-containing constituents.

At the beginning of solidification, the alloy remains in the liquid + (Ni) region, with the first solid phase being an Ni-rich solid solution. The calculated liquidus temperatures are almost identical for the two models, 1344.37°C for the Scheil simulation and 1344.33°C for the Lever simulation. This close agreement confirms that the initial solidification temperature is essentially insensitive to the assumed equilibrium/non-equilibrium solidification conditions.

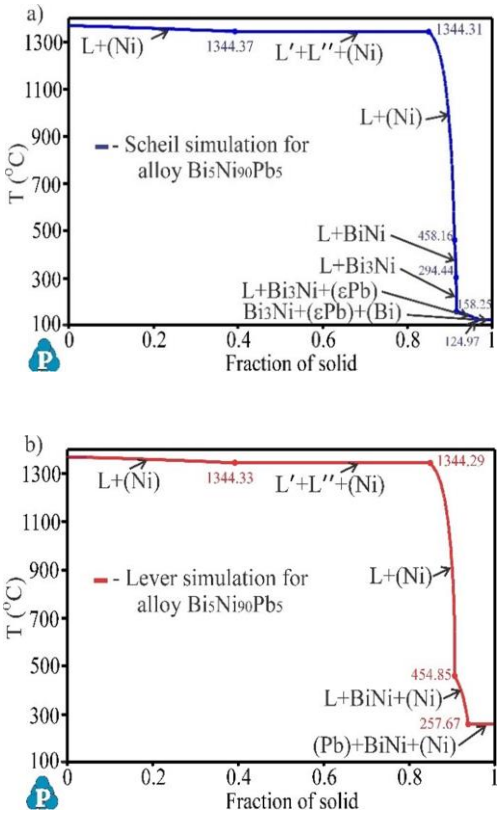


Fig. 13. Scheil (a) and Lever (b) simulation results for alloy $Bi_5Ni_{90}Pb_5$.

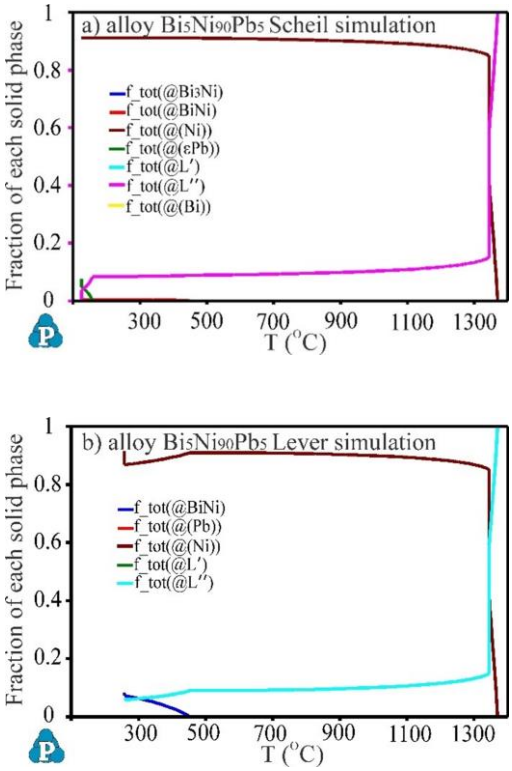


Fig. 14. Fraction of each solid phase as a function of temperature for alloy $Bi_5Ni_{90}Pb_5$: a) Scheil simulation; b) Lever simulation.

As solidification proceeds, the fraction of solid increases rapidly while the temperature remains relatively high. The first significant difference between the two calculations appears at the transition involving the BiNi phase. In the Scheil model, the corresponding temperature is approximately 458.16°C, whereas the Lever model predicts 454.85°C. The Scheil calculation therefore predicts a slightly higher temperature for the onset of this transformation. This difference is associated with the fundamental assumptions of the two models: the Scheil model assumes complete mixing in the liquid and negligible diffusion in the solid, whereas the Lever model represents an equilibrium solidification condition with redistribution between the solid and liquid phases.

A more pronounced difference is observed at lower temperatures. The transition associated with the formation of the BiNi-containing region occurs at approximately 294.44°C in the Scheil calculation, compared with 257.67°C in the Lever calculation. This indicates that the assumed degree of solute redistribution has a significant influence on the final stages of solidification. Under Scheil conditions, solute enrichment in the remaining liquid is enhanced because diffusion in the already formed solid is neglected. Consequently, the residual liquid becomes progressively enriched in elements that are rejected by the primary Ni-rich solid, promoting the formation of secondary and low-temperature constituents.

In the final stage of solidification, both models predict a multiphase microstructure containing BiNi, Ni-rich solid solution, and Pb-rich/Bi-containing phases. The Scheil simulation indicates the formation of a final constituent at approximately

124.97°C, while the Lever calculation terminates at approximately 257.67°C. This difference highlights the stronger segregation predicted by the Scheil approach and suggests that the non-equilibrium model is more sensitive to the enrichment of the residual liquid during the last stages of solidification.

Overall, the two simulations show good agreement in the general solidification path and in the formation of the primary Ni-rich phase. However, their differences become increasingly evident as the fraction of solid approaches unity. The Scheil model predicts stronger chemical segregation and a more complex evolution of the residual liquid, whereas the Lever model provides a more equilibrium-like description of phase formation. Considering that the experimental alloy is expected to undergo limited solid-state diffusion during relatively rapid cooling, the Scheil simulation may provide a more realistic representation of the actual solidification path, particularly with respect to the formation of the final Bi-, Pb- and BiNi-rich constituents.

Additional thermodynamic properties can be derived from the solidification simulations, as illustrated in Figs. 14 and 15.

Figure 14 shows the fraction of each solid phase as a function of temperature, while Fig. 15 presents the latent heat and total heat evolution as a function of temperature. Fig. 14 compares the predicted phase evolution of the $Bi_5Ni_{90}Pb_5$ alloy obtained using Scheil and Lever simulations. Both approaches show similar overall phase evolution, with the Ni-rich, (Ni) solid phase remaining dominant over most of the temperature range. The main differences are observed near the solidification end, where the phase fractions change rapidly. Overall, the two simulations exhibit good qualitative agreement. Fig. 15 presents the heat evolution of the $Bi_5Ni_{90}Pb_5$ alloy as a function of temperature,

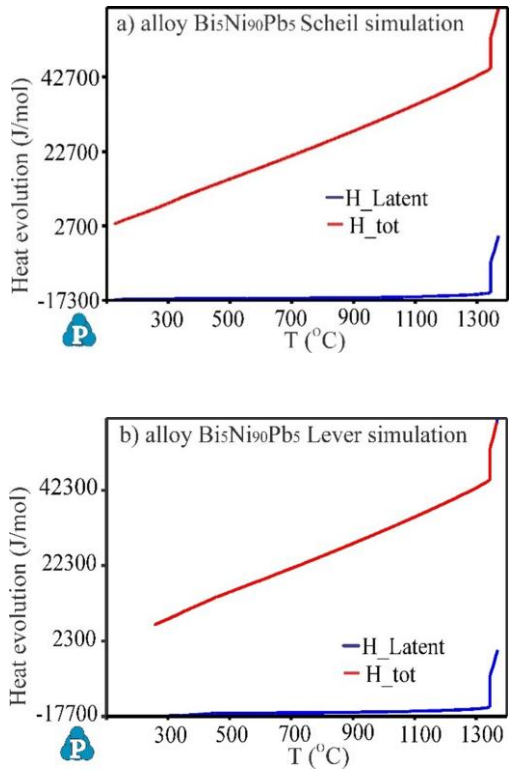


Fig. 15. Heat evolution as a function of temperature for alloy $Bi_5Ni_{90}Pb_5$: a) Scheil simulation; b) Lever simulation.

calculated using Scheil and Lever simulations. Both approaches show a similar trend in the total heat evolution, with a pronounced increase near the end of solidification. The latent heat contribution remains relatively low over most of the temperature range and increases sharply at high temperatures. Overall, the Scheil and Lever simulations exhibit comparable thermal evolution behaviour.

6. Conclusions

Fifteen Bi-Ni-Pb ternary alloys were experimentally investigated using XRD, LOM, SEM–EDS, hardness and electrical conductivity measurements. The experimentally determined phase constitutions showed very good agreement with the calculated 25°C isothermal section, confirming the reliability of the thermodynamic description of the system.

The results demonstrated that both Brinell hardness and electrical conductivity are strongly influenced by phase constitution and phase fractions. The developed Scheffé mixture models provided satisfactory predictive capability, with the special cubic model describing hardness and the quadratic model describing electrical conductivity. The obtained models enable quantitative prediction of the investigated properties within the studied composition range.

Among the investigated alloys, $Bi_5Ni_{90}Pb_5$ exhibited the most favourable combination of hardness and electrical conductivity and was therefore selected for solidification analysis. Scheil and Lever simulations showed similar overall solidification paths, with a primary Ni-rich phase followed by the formation of Bi-Ni intermetallic and Pb-/Bi-rich phases, while the Scheil model predicted stronger segregation during the final stages of solidification.

Overall, the combined thermodynamic, experimental and statistical approach provides a useful basis for understanding composition–phase–property relationships and for further optimisation of Bi-Ni-Pb alloys.

Acknowledgements

The authors would like to thank the Ministry of Science, Technological Development and Innovation of the Republic of Serbia for funding the scientific research work, contract no. 451-03-65/2024-03/200155, realised by the Faculty of Technical Sciences in Kosovska Mitrovica, University of Pristina.

References

[1] Kaňa, V., Krutiš, V., Bořil, P., Záděra, A., & Rimko, M. (2021). Influence of Heat Treatment and Nickel Content on the Properties of the GX4CrNi13-4 Steel. *Archives of Metallurgy and Materials*, 66(1), 37–41. doi: 10.24425/amm.2021.134756

[2] Samui, P., & Agarwal, R. (2022). Thermodynamic Assessment and Solubility of Ni in LBE Coolants. *Thermo*, 2(4), 371–382. doi: 10.3390/thermo2040025

[3] Zeng, Y., Liu, Y., Min, Q., Wen, S., Du, C., Zheng, Z., Liu, H., Du, Y., Premovic, M., & Wang, J. (2020). Diffusion coefficients and atomic mobilities in fcc Ni–Cu–Mo alloys: Experiment and modelling. *Calphad*, 71, 102209. doi: 10.1016/j.calphad.2020.102209

[4] ZaiMi, N.S.M., Salleh, M., BaSer, M., Baharin, N.A.I., Aziz, M.S.A., Abdullah, M.A.B., & Nabiałek, M. (2025). Impact of bismuth as microalloying element in Sn-0.7Cu lead-free solder alloys. *Archives of Metallurgy and Materials*, 70(4), 1753–1758. doi: 10.24425/amm.2025.156258

[5] Milosavljevic, M., Premovic, M., Minic, D., Manasijevic, D., Todic, A., & Tomovic, M. (2021). Thermodynamic description of the Cu-Ge-Pb system: experiment and modeling. *Calphad*, 72, 102216. doi: 10.1016/J.Calphad.2020.102216

[6] Minić, D., Premović, M., Tošković, N., Manasijević, D., Ćosović, V., Janaćković, M., & Tomović, M. (2019). Experimental investigation and thermodynamic calculations of the Bi-Ni-Pb phase diagram. *Journal of Mining and Metallurgy, Section B: Metallurgy*, 55(2), 157–166. doi: 10.2298/JMMB181128024M

[7] Cao, W., Chen, S.L., Zhang, F., Wu, K., Yang, Y., Chang, Y.A., Schmid-Fetzer, R., & Oates, W.A. (2009). PANDAT software with panengine, panoptimizer and panprecipitation for multi-component phase diagram calculation and materials property simulation. *Calphad*, 33(2), 328–342. doi: 10.1016/J.Calphad.2008.08.004

[8] Anderson, M.J., & Whitcomb, P.J. (2016). *RSM simplified: optimizing processes using response surface methods for design of experiments* (2nd ed.). CRC Press.

[9] Myers, R.H., Montgomery, D.C., & Anderson-Cook, C.M. (2016). *Response Surface Methodology, Process and Product Optimization Using Designed Experiments* (4th ed.). Wiley.

[10] Cornell, J.A. (2002). *Experiments with mixtures: designs, models, and the analysis of mixture data* (3rd ed.). Wiley & Sons.

[11] Stat-Ease, (2018). *Handbook for Experimenters*. Stat-Ease. https://cdnm.statease.com/pubs/Handbook%20for%20Experimenters.pdf [accessed 30 Jan. 2025].

[12] Box, G.E.P., & Draper, N.R. (2007). *Response Surfaces, Mixtures, and Ridge Analyses* (2nd ed.). John Wiley & Sons.

[13] Lazić, Ž.R. (2004). *Design of Experiments in Chemical Engineering: A Practical Guide*. Wiley-VCH.

[14] Kang, L., Salgado, J.C., & Brenneman, W.A. (2016). Comparing the Slack-Variable Mixture Model with Other Alternatives. *Technometrics*, 58(2), 255–268. doi: 10.1080/00401706.2014. 985389

[15] Montgomery, D.C. (2017). *Design and Analysis of Experiments* (9th ed.). Wiley.

[16] Davey, W.P. (1925). Precision measurements of the lattice constants of twelve common metals. *Physical Review*, 25(6), 753–761. doi: 10.1103/Physrev.25.753

[17] Owen, E.A. & Yates, E.L. (1936). LXVI. X-Ray measurement of the thermal expansion of pure nickel. *The London, Edinburgh, and Dublin Philosophical Magazine and Journal of Science*, 21(142), 809–819. doi: 10.1080/14786443608561628

[18] Owen, E.A. & Yates, E.L. (1933). XLI. Precision measurements of crystal parameters, *The London, Edinburgh, and Dublin Philosophical Magazine and Journal of Science*, 15(98), 472–488. doi: 10.1080/14786443309462199

[19] Takahashi, T., Mao, H.K., & Bassett, W.A. (1969). Lead: X-ray diffraction study of a high-pressure polymorph. *Science*, 165(3900), 1352–1353. doi: 10.1126/Science.165.3900.13

[20] Martinez Piñeiro, E.L., Ruiz Herrera, B.L., Escudero, R., & Bucio, L. (2011). Possible coexistence of superconductivity and magnetism in intermetallic $Nibi_3$. *Solid State Communications*, 151(6), 425–429. doi: 10.1016/J.Ssc.2011.01.005

[21] Ruck, M. (1999). Die kristallstruktur von BiNi: eine komplexe Ausdünnungsvariante des $InNi_2$-Typs. *Journal of Inorganic and General Chemistry*, 625, 2050–2054. doi: 10.1002/(SICI)1521-3749(199912)625:12<2050::AID-ZAAC2050>3.0.CO;2-R

[22] https://periodictable.com/Properties/A/BrinellHardness.v.html, [accessed 14 Sep. 2019].

[23] https://periodictable.com/Properties/A/ElectricalConductivity.v.html, [accessed 13 Sep. 2019].